Article

Synthesis, Characterization, and Electronic Structures of a Series of Two-Dimensional Trimetallic Cluster Complexes, Ru(CO)(μ-SnPh)[Pt(PBu)], *x* = 0–3

Richard D. Adams, Burjor Captain, Michael B. Hall, Eszter Trufan, and Xinzheng Yang

J. Am. Chem. Soc., **2007**, 129 (40), 12328-12340• DOI: 10.1021/ja074527o • Publication Date (Web): 19 September 2007

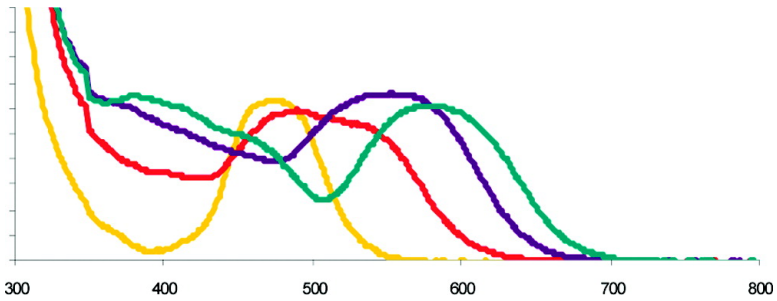

More About This Article

Additional resources and features associated with this article are available within the HTML version:

- Supporting Information
- Links to the 7 articles that cite this article, as of the time of this article download
- Access to high resolution figures
- Links to articles and content related to this article
- Copyright permission to reproduce figures and/or text from this article

View the Full Text HTML

J|A|C|S
ARTICLES
Published on Web 09/19/2007

Synthesis, Characterization, and Electronic Structures of a Series of Two-Dimensional Trimetallic Cluster Complexes, $Ru_3(CO)_9(\mu\text{-}SnPh_2)_3[Pt(PBu^t_3)]_x$, $x = 0-3$

Richard D. Adams,*,† Burjor Captain,† Michael B. Hall,*,‡ Eszter Trufan,† and Xinzheng Yang‡

Contribution from the Department of Chemistry and Biochemistry, University of South Carolina, Columbia, South Carolina 29208, and Department of Chemistry, Texas A&M University, College Station, Texas 77843-3255

Received July 6, 2007; E-mail: Adams@mail.chem.sc.edu

Abstract: The triruthenium-tritin cluster complex, $Ru_3(CO)_9(\mu\text{-}SnPh_2)_3$, **13** was obtained from the reaction of $Ru_3(CO)_{12}$ with Ph_3SnH. Compound **13** reacts with $Pt(PBu^t_3)_2$ to yield three new $Pt(PBu^t_3)$ adducts of **13** $Ru_3(CO)_9(\mu\text{-}SnPh_2)_3[Pt(PBu^t_3)]_x$, **14**−**16** $x = 1 - 3$ formed by the addition of $Pt(PBu^t_3)$ groups to the Ru−Sn bonds. The new complexes form a novel series of trimetallic complexes having planar arrangements of the metal atoms. The UV−vis absorptions of the four complexes shift progressively to longer wavelengths as the number of platinum atoms is added to the cluster. The electronic structures of these complexes have been investigated in the ground and excited states by density functional theory and time-dependent density functional theory, and this has provided a detailed understanding of the metal−metal bonding and electronic transitions that are responsible for their UV−vis absorption properties. The predicted absorption maximum for the model structures for **13**, **14**, **15**, and **16** at 465, 508, 556, and 585 nm differ only 4−18 nm from the experimental values of 474, 490, 552, and 576 nm. The shift of principal UV−vis absorption can be explained by a lowering of the HOMO−LUMO energy gap due to interactions of the platinum atoms with the HOMO and LUMO of the Ru_3Sn_3 core.

Introduction

In recent studies we have shown that the metal phosphine groupings $M(PBu^t_3)$, M = Pd and Pt obtained from the molecules $M(PBu^t_3)_2$, M = Pd and Pt are readily added to the metal−metal bonds of polynuclear metal carbonyl cluster complexes to form electron deficient adducts containing bridging $M(PBu^t_3)$ groups. For example, the reaction of $Pd(PBu^t_3)_2$ with $Ru_3(CO)_{12}$ yielded the tris-$Pd(PBu^t_3)$ adduct $Ru_3(CO)_{12}[Pd(PBu^t_3)]_3$, **1**, by adding a $Pd(PBu^t_3)$ group to each of the three Ru−Ru bonds of the triruthenium cluster.[1]

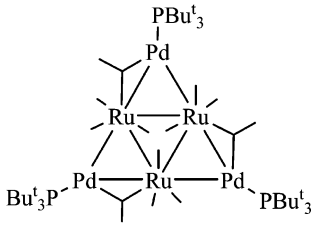

1

On the other hand, the reaction of $Pt(PBu^t_3)_2$ with $Os_3(CO)_{12}$ gives the series of three adducts $Os_3(CO)_{12}[Pt(PBu^t_3)]_n$, **2**, $n = 1$, **3**, $n = 2$, and **4**, $n = 3$, by sequentially adding $Pt(PBu^t_3)$ groups to each of the Os−Os bonds of the triosmium cluster; see Scheme 1.[2] The $Pd(PBu^t_3)$ adducts of $Os_3(CO)_{12}$ were also synthesized, but these are less stable and readily interconvert by addition and elimination of the $Pd(PBu^t_3)$ groups.[3]

With fewer CO ligands, $Pt(PBu^t_3)$ groups will adopt triply bridging positions on metal clusters, as found in the complex $Os_3(CO)_{10}[Pt(PBu^t_3)]_2$, **5**. Interestingly, the unsaturated complex **5** readily activates hydrogen, reversibly, at room temperature and lower to form a series of polyhydride complexes $Os_3(CO)_{10}[Pt(PBu^t_3)]_2(\mu\text{-}H)_2$, **6**, and $Os_3(CO)_{10}[Pt(PBu^t_3)]_2(\mu\text{-}H)_4$, **7**, by opening and closing the metal clusters, see Scheme 2.[4]

In contrast, the highly unsaturated pentanuclear platinum−rhenium cluster complex $Pt_3Re_2(CO)_6(PBu^t_3)_3$, **8**, sequentially adds 3 equiv of hydrogen at room temperature to yield the series of polyhydride complexes $Pt_3Re_2(CO)_6(PBu^t_3)_3(\mu\text{-}H)_2$, **9**, $Pt_3Re_2(CO)_6(PBu^t_3)_3(\mu\text{-}H)_4$, **10**, and $Pt_3Re_2(CO)_6(PBu^t_3)_3(\mu\text{-}H)_6$, **11**, without any metal−metal bond cleavages; see Scheme 3.[5]

We have also found that $Pd(PBu^t_3)$ and $Pt(PBu^t_3)$ groups can also be added to transition metal−main group metal bonds.[6,7] For example, the reaction of $Re_2(CO)_8(\mu\text{-}SnPh_2)_2$ with $Pt(PBu^t_3)_2$

† University of South Carolina.
‡ Texas A&M University.

(1) (a) Adams, R. D.; Captain, B.; Fu, W.; Hall, M. B.; Manson, J.; Smith, M. D.; Webster, C. E. *J. Am. Chem. Soc.* **2004**, *126*, 5253−5267. (b) Adams, R. D.; Captain, B.; Fu, W.; Smith, M. D. *J. Am. Chem. Soc.* **2002**, *124*, 5628−5629.
(2) Adams, R. D.; Captain, B.; Fu, W.; Smith, M. D.; Zhu, L. *Inorg. Chem.* **2006**, *45*, 430−436.
(3) Adams, R. D.; Captain, B.; Zhu, L. *J. Cluster Sci.* **2006**, *17*, 87−95.
(4) Adams, R. D.; Captain, B.; Zhu, L. *J. Am. Chem. Soc.* **2007**, *129*, 2454−2455.
(5) (a) Adams, R. D.; Captain, B.; Beddie, C.; Hall, M. B. *J. Am. Chem. Soc.* **2007**, *129*, 986−1000. (b) Adams, R. D.; Captain, B. *Angew. Chem., Int. Ed.* **2005**, *44*, 2531−2533.

10.1021/ja074527o CCC: $37.00

Scheme 1

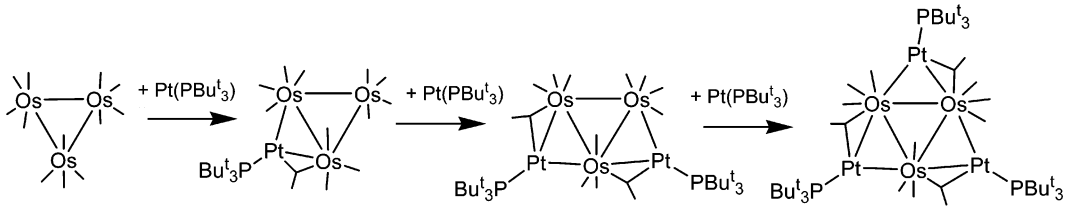

2 **3** **4**

Scheme 2

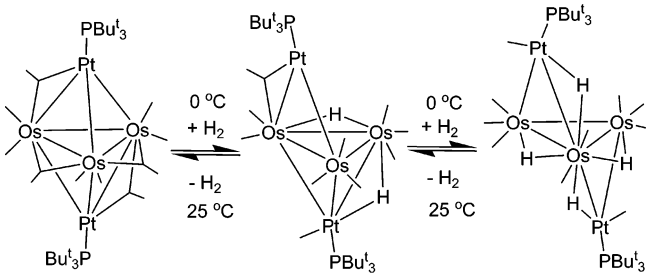

5 **6** **7**

has yielded mono- and bis-Pt(PBu$^t_3$) adducts $Re_2(CO)_8(\mu\text{-}SnPh_2)_2[Pt(PBu^t_3)]_n$, **11**, $n = 1$ and **12**, $n = 2$, Scheme 4.[6]

We have now prepared the triruthenium cluster complex, $Ru_3(CO)_9(\mu\text{-}SnPh_2)_3$, **13** that contains three bridging diphenylstannylene ligands, one across each Ru−Ru bond and have investigated its reactions with Pt(PBu$^t_3$)$_2$. We have isolated three new Pt(PBu$^t_3$) adducts of **13** $Ru_3(CO)_9(\mu\text{-}SnPh_2)_3[Pt(PBu^t_3)]_x$, **14**−**16**, $x = 1-3$ formed by the addition of Pt(PBu$^t_3$) groups to the Ru−Sn bonds about the Ru_3Sn_3 triangle. The new complexes form a novel series of two-dimensional trimetallic cluster complexes that exhibit an interesting pattern of UV−vis absorption properties. Because of the increasing interest and importance of the absorption and emission properties of multinuclear metal complexes[8] and metal containing nanoclusters,[9−10] we have carried out a detailed analysis of the electronic structures of this series of molecules in the ground and excited states by density functional theory and time-dependent density functional theory.[11] The syntheses, characterizations, and investigations of the molecular and electronic structures of **13** and the three new two-dimensional trimetallic complexes **14**−**16** are reported here.

(6) (a) Adams, R. D.; Captain, B.; Herber, R. H.; Johansson, M.; Nowik, I.; Smith, J. L., Jr.; Smith, M. D. *Inorg. Chem.* **2005**, *44*, 6346−6358. (b) Adams, R. D.; Captain, B.; Johansson, M.; Smith, J. L., Jr. *J. Am. Chem. Soc.* **2005**, *127*, 488−489.

(7) Adams, R. D.; Captain, B.; Zhu, L. *Organometallics* **2006**, *25*, 2049−2054.

(8) (a) Lam, W. H.; Cheng, C.-C.; Yam, V. W.-W. *Inorg. Chem.* **2006**, *45*, 9434−9441. (b) Roy, L. E.; Hughbanks, T. *Inorg. Chem.* **2006**, *45*, 8273−8282. (c) Ebihara, M.; Iiba, M.; Higashi, S.; Tsuzuki, N.; Kawamura, T.; Morioka, T.; Ozawa, S.; Yamabe, T.; Masuda, H. *Polyhedron* **2003**, *22*, 3413−3422.

(9) (a) Creighton, J. A.; Eadon, D. G. *J. Chem. Soc., Faraday Trans.* **1991**, *87*, 3881−3891. (b) Link, S.; El-Sayed, M. A. *J. Phys. Chem. B* **1999**, *103*, 4212−4217.

(10) (a) Somers, R. C.; Bawendi, M. G.; Nocera, D. G. *Chem. Soc. Rev.* **2007**, *36*, 579. (b) Klimov, V. I.; Mikhailovsky, A. A.; Xu, S.; Malko, A.; Hollingsworth, J. A.; Leatherdale, C. A.; Eisler, H. J.; Bawendi, M. G. *Science* **2000**, *290*, 314−317. (c) Lopez del Puerto, M.; Tiago, M. L.; Chelikowsky, J. R. *Phys. Rev. Lett.* **2006**, *97*, 96401−4.

(11) (a) Runge, E.; Gross, E. K. U. *Phys. Rev. Lett.* **1984**, *52*, 997−1000. (b) Casida, M. E.; Jamorski, C.; Casida, K. C.; Salahub, D. R. *J. Chem. Phys.* **1998**, *108*, 4439−4449. (c) Stratmann, R. E.; Scuseria, G. E.; Frisch, M. J. *J. Chem. Phys.* **1998**, *109*, 8218−8224.

Experimental Section

General Data. Reagent grade solvents were dried by the standard procedures and were freshly distilled prior to use. Infrared spectra were recorded on a Thermo Nicolet Avatar 360 FT-IR spectrophotometer. ^{1}H, ^{31}P{^{1}H}, and ^{119}Sn NMR spectra were recorded on a Varian Mercury 400 spectrometer operating at 400.1, 161.9, and 149.3 MHz, respectively. ^{31}P{^{1}H} NMR spectra were externally referenced against 85% *ortho*-H_3PO_4. ^{119}Sn NMR spectra were externally referenced against Me_4Sn in C_6D_6 standard (0 ppm). Electrospray mass spectrometric measurements were obtained on a MicroMass Q-Tof spectrometer with an accuracy of ±0.2 Da. Elemental analyses were performed by Desert Analytics (Tucson, AZ). $Ru_3(CO)_{12}$ and bis(tri-*tert*-butylphosphine)-platinum(0), Pt(PBu$^t_3$)$_2$, were obtained from STREM and were used without further purification. Ph_3SnH was purchased from Aldrich and was used without further purification. Product separations were performed by TLC in air on Analtech 0.25 and 0.5 mm silica gel 60 Å F_{254} glass plates.

Synthesis of $Ru_3(CO)_9(\mu\text{-}SnPh_2)_3$, 13. A 30.0 mg amount of $Ru_3(CO)_{12}$ (0.047 mmol) was dissolved in 35 mL of octane in a 100 mL three-neck flask. To the solution was added a 59.0 mg amount of Ph_3SnH (0.168 mmol). The solution was then heated to reflux in the presence of a slow purge with hydrogen. After 45 min, the reaction mixture was cooled and the solvent was removed in vacuo. The product was separated by TLC by using a 6:1 hexane−methylene chloride solvent mixture to yield 12.8 mg (20%) of orange **13**. Spectral data for **13**: IR ν_{CO} (cm^{-1} in hexane): 2046 (m), 2019 (s), 1991 (m). ^{1}H NMR ($CDCl_3$, in ppm) at 25 °C: $\delta = 7.32-7.79$ (m, 30 H, Ph). ^{119}Sn NMR (in CD_2Cl_2, ppm): $\delta = 1016$ (s, $^2J_{^{119}Sn-^{117}Sn} = 766$ Hz). EI/MS *m*/*z*: 1374, M$^+$; 1234, M$^+$ − 5CO; 1206, M$^+$ − 6CO.

Synthesis of $Ru_3(CO)_9(\mu\text{-}SnPh_2)_3[Pt(PBu^t_3)]$, 14, $Ru_3(CO)_9(\mu\text{-}SnPh_2)_3[Pt(PBu^t_3)]_2$, 15, and $Ru_3(CO)_9(\mu\text{-}SnPh_2)_3[Pt(PBu^t_3)]_3$, 16. (a) A 25.5 mg amount of **13** (0.0185 mmol) was dissolved in 30 mL of CH_2Cl_2. To this solution a 16.7 mg amount of Pt(PBu$^t_3$)$_2$ (0.0279 mmol) was added, and the mixture was stirred at room temperature for 6 h. During this time, the color of the solution changed from orange to dark red. The solvent was then removed in vacuo, and the products were separated by TLC by using a 6:1 hexane−methylene chloride solvent mixture to yield in order of elution the following: 13.1 mg of red **14** (40%), purple **15** (3.4 mg, 9%), and blue-gray **16** (0.1 mg, 0.2%). Spectral data for **14**: IR ν_{CO} (cm^{-1} in CH_2Cl_2): 2074 (w), 2037 (m), 2007 (vs), 1978 (w), 1784(w). ^{1}H NMR ($CDCl_3$, in ppm) at 25 °C: $\delta = 7.26-7.83$ (m, 30 H, Ph), 1.24 (d, 27 H, CH_3, $^3J_{P-H} = 13$ Hz). ^{31}P{^{1}H}NMR ($CDCl_3$, in ppm) at 25 °C: $\delta = 110$ (s, 1 P, $^1J_{Pt-P} = 5911$ Hz). ES/MS *m*/*z*: 1852, M$^+$ + K + NCMe; 1811, M$^+$ + K. Spectral data for **15**: IR ν_{CO} (cm^{-1} in CH_2Cl_2): 2063 (w), 2024 (m), 1998 (vs), 1968 (w), 1784 (w). ^{1}H NMR ($CDCl_3$, in ppm) at 25 °C: $\delta = 7.22-7.93$ (m, 30 H, Ph), 1.21 (d, 54 H, CH_3, $^3J_{P-H} = 13$ Hz). ^{31}P{^{1}H}NMR ($CDCl_3$, in ppm) at 25 °C: $\delta = 109.31$ (s, 2 P, $^1J_{Pt-P} = 5944$ Hz). ES/MS *m*/*z*: 2209, M$^+$ + NCMe; 2092, M$^+$ − C_6H_6. Spectral data for **16** : IR ν_{CO} (cm^{-1} in CH_2Cl_2): 2010 (w, sh), 1987 (s), 1778 (w). ^{1}H NMR ($CDCl_3$, in ppm) at 25 °C: $\delta = 7.14-7.98$ (m, 30 H, Ph), 1.16 (d, 81 H, CH_3, $^3J_{P-H} = 13$ Hz). ^{31}P{^{1}H}NMR ($CDCl_3$, in ppm) at 25 °C: $\delta = 108$ (s, 3 P, $^1J_{Pt-P} = 5934$ Hz). Elemental analysis (%) calcd: 37.91, C; 4.36, H. Found: 38.86, C; 4.27, H.

Scheme 3

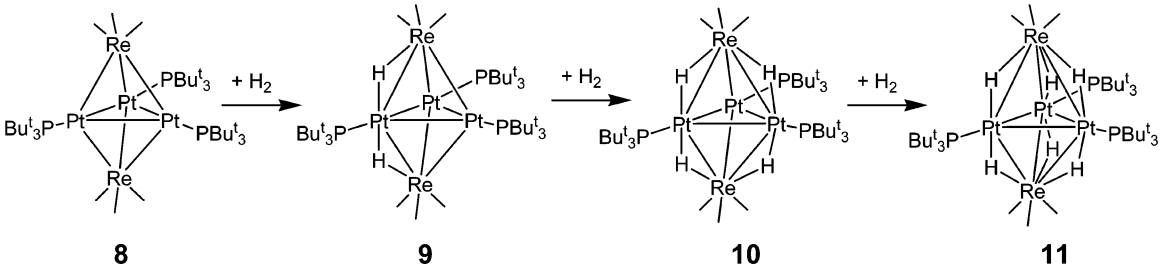

Scheme 4

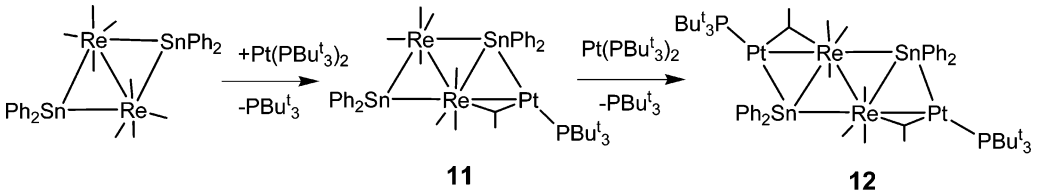

Table 1. Experimental UV−vis Absorption Data and TDDFT Calculated HOMO−LUMO Transition Wavelengths for Compounds **13**−**16**

compd	concn[a] (×10^{-5} mol/L)	λ_{max} (nm)	ϵ (L·mol^{-1}·cm^{-1})	predicted λ_{max} (nm)
13	6.99	474	9080	465
14	7.00	490	8460	508
15	6.98	552	9450	556
16	6.81	576	9000	585

[a] Spectra were recorded in CH_2Cl_2 solvent.

(b) A 16.7 mg amount of **13** (0.012 mmol) was dissolved in 30 mL of CH_2Cl_2. To this solution a 21.8 mg amount of Pt(PBu$^t_3$)$_2$ (0.0364 mmol) was added, and the mixture was stirred at room temperature for 12 h. During this time, the color of the solution changed from orange to dark purple. The solvent was then removed *in vacuo*, and the products were separated by TLC by using a 6:1 hexane−methylene chloride solvent to yield in order of elution: **14** (1.8 mg; 8% yield); 8.9 mg of **15** (34% yield); and **16** (0.2 mg; 0.6%).

UV−vis Measurements. UV−vis spectra were recorded on a Varian model Cary 500 Scan UV−vis/near-IR spectrophotometer. Accurately weighed amounts of the compounds were dissolved in freshly distilled methylene chloride and placed in quartz cuvettes. The concentrations of the solutions ranged from 6.8×10^{-5} to 7.0×10^{-5} mol/L. The peak maxima and the corresponding absorbance values were identified for each compound, and the extinction coefficients were calculated according to Beer's Law. The results are listed in Table 1.

Crystallographic Analyses. Single crystals of **13** and **16** suitable for X-ray diffraction analysis were obtained by slow evaporation of solvent from solutions in methylene chloride/hexane solvent mixtures at 5 °C. Single crystals of **14** and **15** suitable for X-ray diffraction analysis were obtained by slow evaporation of solvent from solutions in methylene chloride/hexane solvent mixtures at −20 °C. Each data crystal was glued onto the end of a thin glass fiber. X-ray intensity data were measured by using a Bruker SMART APEX CCD-based diffractometer using Mo Kα radiation ($\lambda = 0.710\ 73$ Å). The raw data frames were integrated with the SAINT+ program by using a narrow-frame integration algorithm.[1] Correction for Lorentz and polarization effects were also applied with SAINT+. An empirical absorption correction based on the multiple measurement of equivalent reflections was applied by using the program SADABS. All structures were solved by a combination of direct methods and difference Fourier syntheses and refined by full-matrix least squares on F^2, by using the SHELXTL software package.[2] Unless indicated otherwise, below, all non-hydrogen atoms were refined with anisotropic thermal parameters. Hydrogen atoms were placed in geometrically idealized positions and included as standard riding atoms during the least-squares refinements. Crystal data, data collection parameters, and results of the refinements are listed in Table 2.

Compounds **13** and **15** crystallized in the monoclinic crystal system. The systematic absences in the intensity data identified the unique space group $P2_1/n$. For compound **13** there are two independent formula equivalents of the complex present in the asymmetric unit. For compound **15** one-half of a molecule of hexane from the crystallization solvent cocrystallized with the complex. The solvent molecule lies on a center of inversion and was refined with isotropic thermal parameters.

Compound **14** crystallized in the triclinic crystal system. The space group $P\bar{1}$ was assumed and confirmed by the successful refinement and solution of the structure. The quaternary carbons on the tri-*tert*-butyl phosphine ligand were disordered over two orientations and were refined in the ratio 50/50. The carbon atoms of the tri-*tert*-butyl phosphine ligand were refined with isotropic thermal parameters. One molecule of methylene chloride from the crystallization solvent cocrystallized with the complex. The solvent molecule was included in the analysis and was refined with isotropic thermal parameters.

Compound **16** crystallized in the hexagonal crystal system. Systematic absences indicated the space groups $P6_3$ and $P6_3/m$, the latter of which was confirmed by the successful solution and refinement of the structure. With $Z = 2$, the molecule lies on a $\bar{6}$ symmetry site and has overall C_{3h} symmetry. The crystal packing of the molecules of **16** contains voids that are filled with disordered molecules from the crystallization solvent. Despite many attempts, no reasonable disorder model for these solvent molecules could be obtained. In the final stages of the refinements the largest peak in the final difference Fourier map was 2.190 e$^-$/Å^3, with satisfactory low R factors, $R_1 = 3.66\%$.

Theoretical Section

Geometry Structure Optimization. The four complexes, designated as Ru_3Sn_3, $Ru_3Sn_3Pt_1$, $Ru_3Sn_3Pt_2$, and $Ru_3Sn_3Pt_3$, represent the $[Ru(CO)_3]_3[Sn(C_6H_5)_2]_3$ cluster with three different numbers of Pt−P^{t}Bu$_3$ groups attached. Since phenyl and *tert*-butyl contain large numbers of atoms which contribute very little to the low-lying excited states of the whole clusters, these groups were replaced by H for these structures in the calculations. This simplification in structure reduces the required computational resources dramatically. All geometries of these simplified models were optimized separately by using density functional theory[14,15]

(12) *SAINT+*, version 6.2a. Bruker Analytical X-ray System, Inc.: Madison, Wisconsin, U.S.A., 2001.
(13) Sheldrick, G. M. *SHELXTL*, version 6.1; Bruker Analytical X-ray Systems, Inc.: Madison, Wisconsin, U.S.A., 1997.

Table 2. Crystallographic Data for Compounds **13**−**16**

	13	**14**	**15**	**16**
empirical formula	$Ru_3Sn_3O_9C_{45}H_{30}$	$PtRu_3Sn_3PO_9C_{57}H_{57}\cdot 1.0\ CH_2Cl_2$	$Pt_2Ru_3Sn_3P_2O_9C_{69}H_{84}\cdot {}^1/_2C_6H_{14}$	$Pt_3Ru_3Sn_3O_9C_{81}H_{111}$
formula weight	1373.97	1856.29	2211.85	2566.16
crystal system	monoclinic	triclinic	monoclinic	hexagonal
lattice parameters				
a (Å)	24.8837(11)	13.7703(4)	18.3260(8)	18.5176(2)
b (Å)	16.4642(7)	13.9457(4)	18.6782(8)	18.5176(2)
c (Å)	25.8863(11)	19.3885(6)	23.4249(10)	16.4848(3)
α (deg)	90	77.485(1)	90	90
β (deg)	117.634(1)	85.194(1)	101.171(1)	90
γ (deg)	90	61.818(1)	90	120
V (Å^3)	9395.6(7)	3203.18(16)	7866.3(6)	4895.35(12)
space group	$P2_1/n$ (#14)	$P\bar{1}$ (#2)	$P2_1/n$ (#14)	$P6_3/m$ (#176)
Z value	8	2	4	2
ρ_{calcd} (g/cm^3)	1.943	1.925	1.868	1.741
μ (Mo Kα) (mm^{-1})	2.561	4.172	5.128	5.563
temperature (K)	294(2)	294(2)	294(2)	294(2)
$2\Theta_{max}$ (deg)	50.06	56.66	50.06	56.60
no. obsd ($I > 2\sigma(I)$)	9257	12872	8898	3369
no. parameters	1081	639	805	171
goodness of fit	1.000	1.046	1.018	1.187
max shift in cycle	0.003	0.001	0.001	0.001
residuals:[a] R1; wR2	0.0485; 0.0878	0.0379; 0.1045	0.0457; 0.0880	0.0366; 0.1263
absorption correction,	multiscan	multiscan	multiscan	multiscan
max/min	1.000/0.575	1.000/0.732	1.000/0.475	1.000/0.424
largest peak in final diff. map (e$^-$/Å^3)	0.966	1.792	1.411	2.190

[a] $R = \Sigma_{hkl}(||F_{obsd}| - |F_{calcd}||)/\Sigma_{hkl}|F_{obsd}|$; $R_w = [\Sigma_{hkl}w(|F_{obsd}| - |F_{calcd}|)^2/\Sigma_{hkl}wF_{obsd}^2]^{1/2}$, $w = 1/\sigma^2(F_{obsd})$; GOF $= [\Sigma_{hkl}w(|F_{obsd}| - |F_{calcd}|)^2/(n_{data} - n_{vari})]^{1/2}$.

(DFT) at the Tao−Perdew−Staroverov−Scuseria[16] (TPSS) meta-GGA level. All-electron 6-31+G(d,p) basis sets[17] were used for H, C, O, and P atoms. Relativistic effects of heavy metal atoms were considered by using the relativistic effect-core-potential (ECP) basis set SDB-aug-cc-pVTZ[18] for Sn and Stuttgart RSC 1997 ECP + 2f1g[18,19] for Ru and Pt. The geometric structures of Ru_3Sn_3 and $Ru_3Sn_3Pt_3$ clusters were restricted to the D_{3h} and C_{3h} point group symmetry, respectively, while the point groups of $Ru_3Sn_3Pt_1$ and $Ru_3Sn_3Pt_2$ clusters were C_1.

Excited-State Calculations. Six vertical excited energies of these clusters were calculated by using time-dependent density functional theory (TDDFT)[11] with the same basis sets and exchange-correlation functional as those used for the optimized structures. TDDFT provides a formally rigorous extension of the Hohenberg−Kohn−Sham density functional theory, which is time-independent, to the situation where a system is subject to a time-dependent perturbation modifying its external potential.[20] The transitions to triplet and higher order multiplet excited states from the ground state are forbidden because the ground states of these clusters are singlets. Even if there are some transitions from higher order multiplet excited states to the ground state caused by spin−orbit splitting, these transitions should be very weak in strength relative to the transitions to the singlet excited states. Therefore, the detailed effects of spin−orbit coupling do not need to be considered in the calculations for the transitions of interest.

Molecular Orbital Analysis. All molecular orbital analyses are based on single point calculations performed by using the ADF 2006 program[21] with the Perdew−Burke−Ernzerhof (PBE)[22] density functional at the previously optimized geometries. All-electron Slater-type quadruple-ζ basis sets with four polarization functions (QZ4P) were used for all atoms. The zeroth-order regular approximate relativistic equation (ZORA)[23] was used for the relativistic-effect correction. The built-in fragment oriented approach in ADF simplifies the analysis of the relationship between cluster orbitals and orbitals of the fragments that make up the final clusters.

Results and Discussion

Compound **13** was obtained in 20% yield from the reaction of $Ru_3(CO)_{12}$ with Ph_3SnH in an octane solution at reflux (125 °C) under a hydrogen atmosphere. Compound **13** was characterized by IR, ^{1}H and ^{119}Sn NMR, mass spectrometry, and single-crystal X-ray diffraction analysis. Compound **13** crystallizes with two independent molecules in the crystallographic asymmetric unit. Both molecules are structurally similar. An ORTEP diagram of the molecular structure of one of the two molecules is shown in Figure 1. The compound consists of a triangular cluster of three ruthenium atoms with three bridging diphenylstannylene ligands, $SnPh_2$, one on each of the three Ru−Ru bonds of the cluster. The tin atoms of the $SnPh_2$ ligands lie essentially in the plane of the Ru_3 triangle. Each ruthenium atom contains three linear terminal carbonyl ligands, two lie perpendicular to the plane of the cluster, while

(14) All calculations were conducted using the Gaussian03 suite of programs: Frisch, M. J., et al. *Gaussian 03*, revision B.4; Gaussian, Inc.: Pittsburgh, PA, 2003.
(15) (a) Hohenberg, P.; Kohn, W. *Phys. Rev.* **1964**, *136*, B864−B871. (b) Kohn, W.; Sham, L. J. *Phys. Rev.* **1965**, *140*, A1133−A1138.
(16) Tao, J. M.; Perdew, J. P.; Staroverov, V. N.; Scuseria, G. E. *Phys. Rev. Lett.* **2003**, *91*, 146401−4.
(17) (a) Hehre, W. J.; Ditchfield, R.; Pople, J. A. *J. Chem. Phys.* **1972**, *56*, 2257−2261. (b) Francl, M. M.; Petro, W. J.; Hehre, W. J.; Binkley, J. S.; Gordon, M. S.; DeFrees, D. J.; Pople, J. A. *J. Chem. Phys.* **1982**, *77*, 3654−3665. (c) Clark, T.; Chandrasekhar, J.; Spitznagel, G. W.; Schleyer, P. V. R. *J. Comput. Chem.* **1983**, *4*, 294−301. (d) Hariharan, P. C.; Pople, J. A. *Theor. Chim. Acta* **1973**, *28*, 213−222.
(18) Martin, J. M. L.; Sundermann, A. *J. Chem. Phys.* **2001**, *114*, 3408−3420.
(19) Andrae, D.; Haeussermann, U.; Dolg, M.; Stoll, H.; Preuss, H. *Theor. Chim. Acta* **1990**, *77*, 123−141.
(20) (a) Marques, M. A. L.; Gross, E. K. U. *Annu. Rev. Phys. Chem.* **2004**, *55*, 427−455. (b) Burke, K.; Werschnik, J.; Gross, E. K. U. *J. Chem. Phys.* **2005**, *123*, 062206−9.
(21) The ADF, version 2006.01, package of programs for first-principles electronic structure calculations. Baerends, E. J. et al. *Scientific Computing & Modelling*; Amsterdam, Netherlands, 2005; http://www.scm.com/.
(22) (a) Perdew, J. P.; Burke, K.; Ernzerhof, M. *Phys. Rev. Lett.* **1996**, *77*, 3865−3868. (b) Perdew, J. P.; Burke, K.; Ernzerhof, M. *Phys. Rev. Lett.* **1997**, *78*, 1396.
(23) (a) van Lenthe, E.; Baerends, E. J.; Snijders, J. G. *J. Chem. Phys.* **1993**, *99*, 4597. (b) van Lenthe, E.; Baerends, E. J.; Snijders, J. G. *J. Chem. Phys.* **1994**, *101*, 9783. (c) van Lenthe, E.; Ehlers, A. E.; Baerends, E. J. *J. Chem. Phys.* **1999**, *110*, 8943.

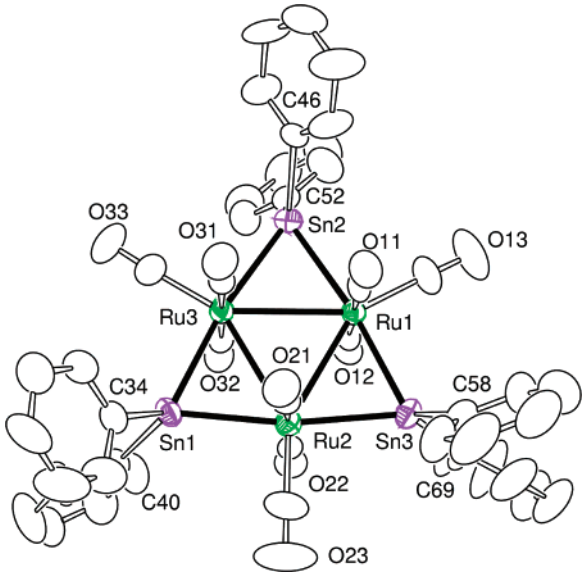

Figure 1. An ORTEP diagram of the molecular structure of $Ru_3(CO)_9(\mu\text{-}SnPh_2)_3$, **13**, showing 40% probability thermal ellipsoids. Selected interatomic distances (Å) are as follows: (for molecule 1) Ru(1)−Ru(3) = 2.9620(10), Ru(1)−Ru(2) = 2.9688(10), Ru(2)−Ru(3) = 3.0022(10), Ru(1)−Sn(2) = 2.6509(10), Ru(1)−Sn(3) = 2.6617(10), Ru(2)−Sn(1) = 2.6551(10), Ru(2)−Sn(3) = 2.6564(10), Ru(3)−Sn(1) = 2.6352(9), Ru(3)−Sn(2) = 2.6499(9); (for molecule 2) Ru(4)−Ru(5) = 2.9585(10), Ru(4)−Ru(6) = 3.0180(10), Ru(5)−Ru(6) = 2.9625(10), Ru(4)−Sn(4) = 2.6477(10), Ru(4)−Sn(5) = 2.6545(10), Ru(5)−Sn(6) = 2.6391(9), Ru(5)−Sn(4) = 2.6450(9), Ru(6)−Sn(5) = 2.6489(9), Ru(6)−Sn(6) = 2.6506(9).

one lies in the plane of the cluster. The Ru−Ru bond distances range from 2.9585(10) to 3.0180(10) Å. These distances are significantly longer than the Ru−Ru bond distances found in $Ru_3(CO)_{12}$, Ru−Ru = 2.854(1) Å,[24] but are similar to the Ru−Ru distances, 2.887(2)−2.977(2) Å, that were observed for the related Ru_3Sn_3 cluster complexes, $Ru_3(CO)_9[\mu\text{-}Sn(C_6H_2Pr^i_3)_2]_{3-x}[\mu\text{-}Sn\{CH(SiMe_3)\}_2]_x$, **17**−**19**, $x = 0-2$ that have been obtained from reactions of $Ru_3(CO)_{12}$ with the stannylenes $Sn(C_6H_2Pr^i_3)_2$ and $Sn\{CH(SiMe_3)_2$.[25] In previous studies, it was shown that metal−metal bonds are increased in length because of strong bonding interactions to bridging $SnPh_2$ ligands.[6] The Ru−Sn distances in **13** range from 2.6352(9) to 2.6617(10) Å. These values are significantly shorter than the Ru−Sn bond distances in **17**−**19**, 2.691(2) to 2.750(2) Å. The longer Ru−Sn distances observed in **17**−**19** are probably due to increased steric interactions caused by the bulkier stannylene ligands in these molecules. The ^{119}Sn NMR spectrum of **13** exhibits a highly deshielded singlet at $\delta = +1016$ with coupling to a ^{117}Sn isotope from a neighboring tin ligand, $^2J_{^{119}Sn-^{117}Sn} = 766$ Hz. The chemical shifts of ^{119}Sn span a wide range.[26] Divalent dialkylstannylenes are highly deshielded, *ca* +2300 ppm.[26a] When they are bonded to two metal atoms they are much more shielded, *ca.* 85−125 ppm,[27] but in **13** the metal atoms are also mutually bonded.

Three products were obtained from the reaction of $Pt(PBu^t_3)_2$ with **13**. These were identified as $Ru_3(CO)_9(\mu\text{-}SnPh_2)_3[Pt(PBu^t_3)]_x$, **14**−**16**, $x = 1-3$. The yields vary depending on the amount of $Pt(PBu^t_3)_2$ that is supplied. When the ratio of $Pt(PBu^t_3)_2$/**13** is 1.5:1 in the reaction mixture, compound **14** is the major product and the yields of **14**, **15**, and **16** are 40%, 9%, and 0.2%, respectively. However, when the ratio of $Pt(PBu^t_3)_2$/**13** is increased to 3:1 in the reaction mixture, compound **15** is the major product and the yields of **14**, **15**, and **16** are 8%, 34%, and 0.6%, respectively. The yield of **16** is always very low even when the ratio of $Pt(PBu^t_3)_2$/**13** is as high as 10:1 in the reaction. This may be due to unfavorable steric effects when three $Pt(PBu^t_3)$ groups are added to the Ru_3Sn_3 cluster. In fact, when **16** is dissolved, it slowly loses a $Pt(PBu^t_3)$ group and small amounts of compound **15** form spontaneously.

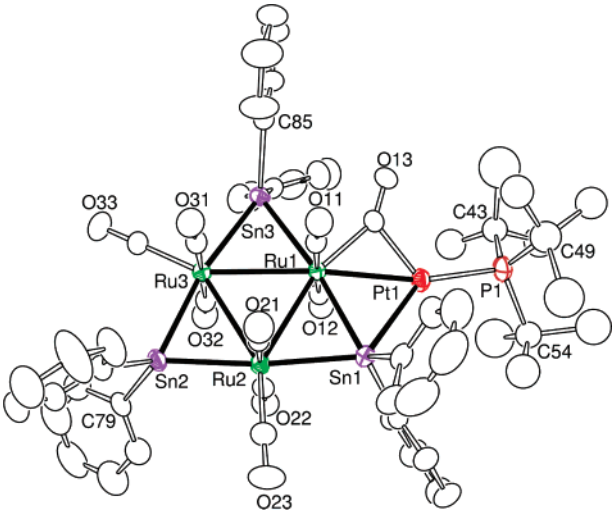

Figure 2. An ORTEP diagram of the molecular structure of $Ru_3(CO)_9(\mu\text{-}SnPh_2)_3[Pt(PBu^t_3)]$, **14**, showing 40% probability thermal ellipsoids. Selected interatomic distances (Å) and angles (deg) are as follows: Ru(1)−Ru(2) = 2.9554(5), Ru(1)−Ru(3) = 2.9970(5), Ru(2)−Ru(3) = 2.9842(5), Pt(1)−Ru(1) = 2.7413(4), Pt(1)−Sn(1) = 2.7804(4), Ru(1)−Sn(3) = 2.6447(5), Ru(1)−Sn(1) = 2.6843(5), Ru(2)−Sn(2) = 2.6299(5), Ru(2)−Sn(1) = 2.6928(5), Ru(3)−Sn(3) = 2.6404(5), Ru(3)−Sn(2) = 2.6667(5), Pt(1)−P(1) = 2.3101(14), Ru(1)−C(13) = 1.991(5), Pt(1)−C(13) = 1.971(6); Pt(1)−C(13)−O(13) = 125.3(4), Ru(1)−C(13)−O(13) = 147.1(5)

All three products were characterized by single-crystal X-ray diffraction analyses, and ORTEP diagrams of the molecular structures of **14**−**16** are shown in Figures 2−4, respectively. Compound **14** contains a central unit of $Ru_3(CO)_9(\mu\text{-}SnPh_2)_3$ with a $Pt(PBu^t_3)$ group bridging its Ru(1)−Sn(1) bond. The platinum atom lies essentially in the plane of the six metal atoms Ru_3Sn_3. The Ru−Ru bond distances are similar in length to those found in **13**, but the Ru(1)−Ru(2) bond distance, 2.9554(5) Å, is significantly shorter than the other two Ru−Ru bonds, Ru(1)−Ru(3) = 2.9970(5) Å and Ru(2)−Ru(3) = 2.9842(5) Å. The platinum bridged Ru−Sn bond, Ru(1)−Sn(1) = 2.6843(5) Å, is significantly longer than all the Ru−Sn bond distances in **13** and **14** except the Ru−Sn bond adjacent to it, Ru(2)−Sn(1) which is 2.6928(5) Å. Similar M−Sn bond lengthening effects were also observed in the compounds **11**, **12**, and $Os_3(CO)_9(\mu\text{-}SnPh_2)_3[Pt(PBu^t_3)]$, **20**. Compound **20**, which has a structure similar to that for **14**, was obtained from the reaction of $Os_3(CO)_9(\mu\text{-}SnPh_2)_3$ with $Pt(PBu^t_3)_2$.[7] A CO ligand on one of the ruthenium atoms, C(13)−O(13), has adopted a strong semibridging position to the platinum atom, Pt(1)−C(13) = 1.971(6) Å and Pt(1)−Ru(1) = 2.7413(4) Å. The tin atom Sn(1) has a five coordinate geometry being bonded to two phenyl

(24) Churchill, M. R.; Hollander, F. J.; Hutchinson, J. P. *Inorg. Chem.* **1977**, *16*, 2655−2659.
(25) Cardin, C. J.; Cardin, D. J.; Convery, M. A.; Dauter, Z.; Fenske, D.; Devereux, M. M.; Power, M. B. *J. Chem. Soc., Dalton Trans.* **1996**, 1133−1144.
(26) (a) Wrackmeyer, B. *Annu. Rep. NMR Spectrosc.* **1999**, *38*, 203−264. (b) Wrackmeyer, B. *Annu. Rep. NMR Spectrosc.* **1985**, *16*, 73−186.
(27) Wrackmeyer, B.; Distler, B.; Herberhold, M. *Z. Naturforsch.* **1992**, *47b*, 1749−1753.

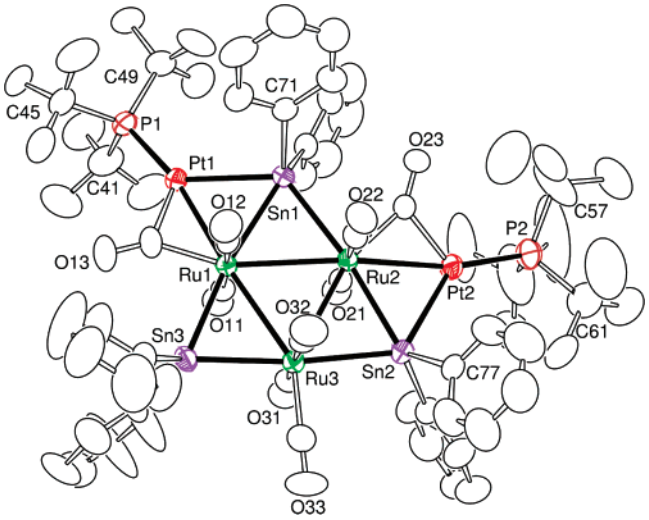

Figure 3. An ORTEP diagram of the molecular structure of $Ru_3(CO)_9(\mu\text{-}SnPh_2)_3[Pt(PBu^t_3)]_2$, **15**, showing 40% probability thermal ellipsoids. Selected interatomic distances (Å) and angles (deg) are as follows: Ru(1)−Sn(3) = 2.6428(19), Ru(1)−Sn(1) = 2.6959(18), Ru(1)−Pt(1) = 2.7508(16), Ru(1)−Ru(3) = 2.970(2), Ru(1)−Ru(2) = 3.0096(18), Ru(2)−Sn(2) = 2.6742(18), Ru(2)−Sn(1) = 2.6766(18), Ru(2)−Pt(2) = 2.7429(14), Ru(2)−Ru(3) = 2.9633(19), Ru(3)−Sn(3) = 2.6181(18), Ru(3)−Sn(2) = 2.6953(18), Pt(1)−Sn(1) = 2.7470(14), Pt(2)−Sn(2) = 2.7922(15), Pt(1)−P(1) = 2.311(5), Pt(2)−P(2) = 2.312(6), Pt(1)−C(13) = 1.956(12), Pt(2)−C(23) = 1.963(10), Ru(1)−C(13) = 1.964(11), Pt(1)−C(13) = 1.956(12), Ru(2)−C(23) = 1.984(10), Pt(2)−C(23) = 1.963(10); Pt(1)−C(13)−O(13) = 125.5(9), Ru(1)−C(13)−O(13) = 145.3(10), Pt(2)−C(23)−O(23) = 125.1(8), Ru(2)−C(23)−O(23) = 146.6(8)

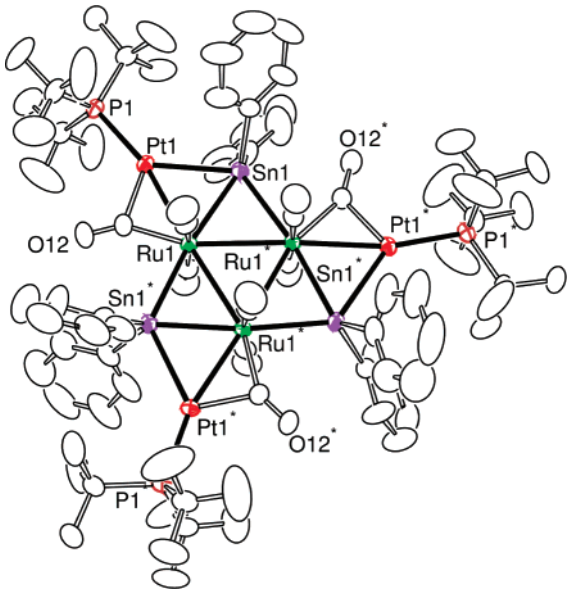

Figure 4. An ORTEP diagram of the molecular structure of $Ru_3(CO)_9(\mu\text{-}SnPh_2)_3[Pt(PBu^t_3)]_3$, **16**, showing 40% probability thermal ellipsoids. Selected interatomic distances (Å) and angle (deg) are as follows: Ru(1)−Ru(1*) = 2.9817(10), Pt(1)−Ru(1) = 2.7606(6), Ru(1)−Sn(1) = 2.6635(9), Ru(1)−Sn(1) = 2.6816(8), Pt(1)−Sn(1) = 2.7433(7), Pt(1)−P(1) = 2.309(2), Ru(1)−C(12) = 1.979(10), Pt(1)−C(12) = 1.974(11); Pt(1)−C(12)−O(12) = 123.5(9), Ru(1)−C(12)−O(12) = 147.9(10).

groups and three metal atoms, Ru(1), Ru(2), and Pt(1), Pt(1)−Sn(1) = 2.7804(4) Å.

Compound **15** is structurally similar to **13** and **14** except that it contains two $Pt(PBu^t_3)$ groups bridging Ru−Sn bonds, Ru(1)−Sn(1) and Ru(2)−Sn(2). The Ru−Ru bond distances are similar to those in **13** and **14**. As in **14**, that addition of platinum

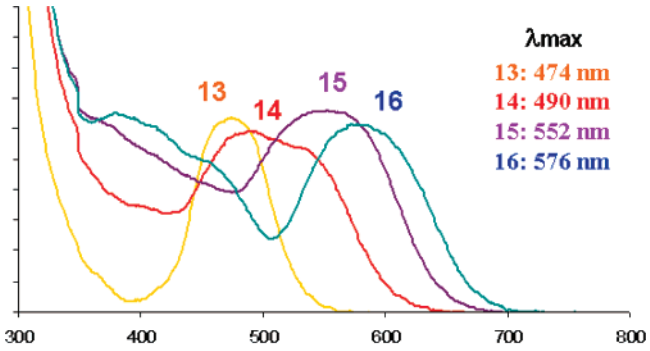

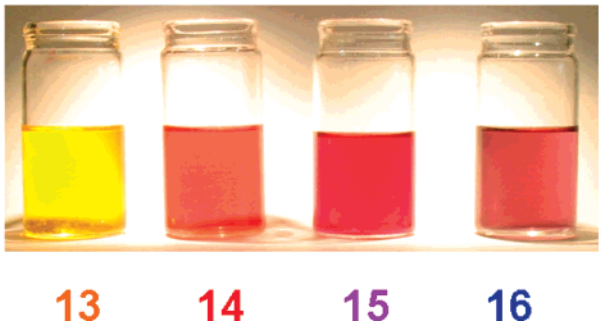

Figure 5. (Top) UV−vis absorption spectra for compounds **13**−**16**. (Bottom) Photograph of the corresponding solutions of **13**−**16** in CH_2Cl_2 solvent in vials.

atoms to the Ru−Sn bonds causes an increase in length of all associated Ru−Sn bonds. The platinum atoms are bonded to the $SnPh_2$ ligands, Pt(1)−Sn(1) = 2.7470(14) Å, Pt(2)−Sn(2) = 2.7922(15) Å, and a CO ligand bridges from a ruthenium atom to each added platinum atom, Pt(1)−C(13) = 1.956(12) Å and Pt(2)−C(23) = 1.963(10) Å.

Compound **16** crystallized in the hexagonal space group $P6_3/m$ with only two formula equivalents of the molecule in the unit cell. The molecule lies on a $\bar{6}$ site and has C_{3h} symmetry; that is, it has both C_3 symmetry and is also crystallographically planar. All nine metal atoms lie in the same plane. The one independent Ru−Ru distance, Ru(1)−Ru(1*) = 2.9817(10) Å, is similar in length to those in **13**−**15**. The Pt−Ru, Ru−Sn, and Pt−Sn distances, 2.7606(6), 2.6635(9), 2.6816(8), and 2.7433(7) Å, respectively, are also very similar to those in **13**−**15**.

UV−vis Absorption Spectra. The series of complexes **13**−**16** present a uniform progression of two-dimensional cluster growth from six to nine metal atoms. Interestingly, solutions of the compounds exhibit a smooth change in color from yellow for **13** (λ_{max}, 475 nm) to a red-blue for **16** (λ_{max}, 576 nm) due to shifts of their absorption bands to longer wavelengths as the number of metal atoms is increased; see Figure 5 and Table 1. Because of the structural similarities of the molecules, we have performed molecular orbital calculations for the entire series in order to understand the electronic and excited-state structures of these molecules and to explain the electronic transitions that are responsible for the UV−vis absorptions in them. The predicted absorption peak (HOMO−LUMO transitions) wavelengths are also listed in Table 1, and the simulated spectra are shown in Figure 6. In order to understand the spectra in detail, we have investigated the electronic structures and bonding in these clusters by building them from their fragments.

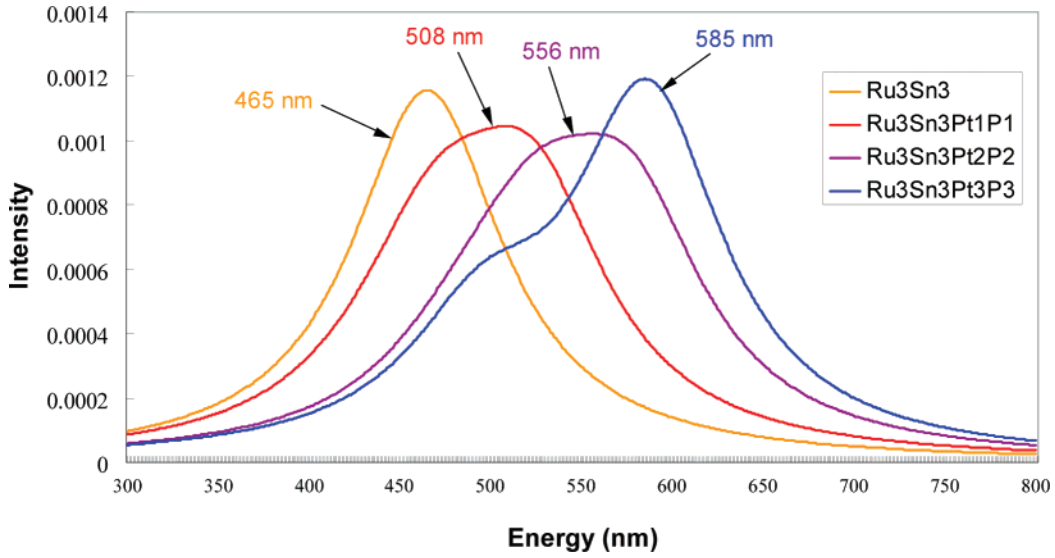

Figure 6. Simulated electronic spectra from TDDFT calculations with 100 nm width.

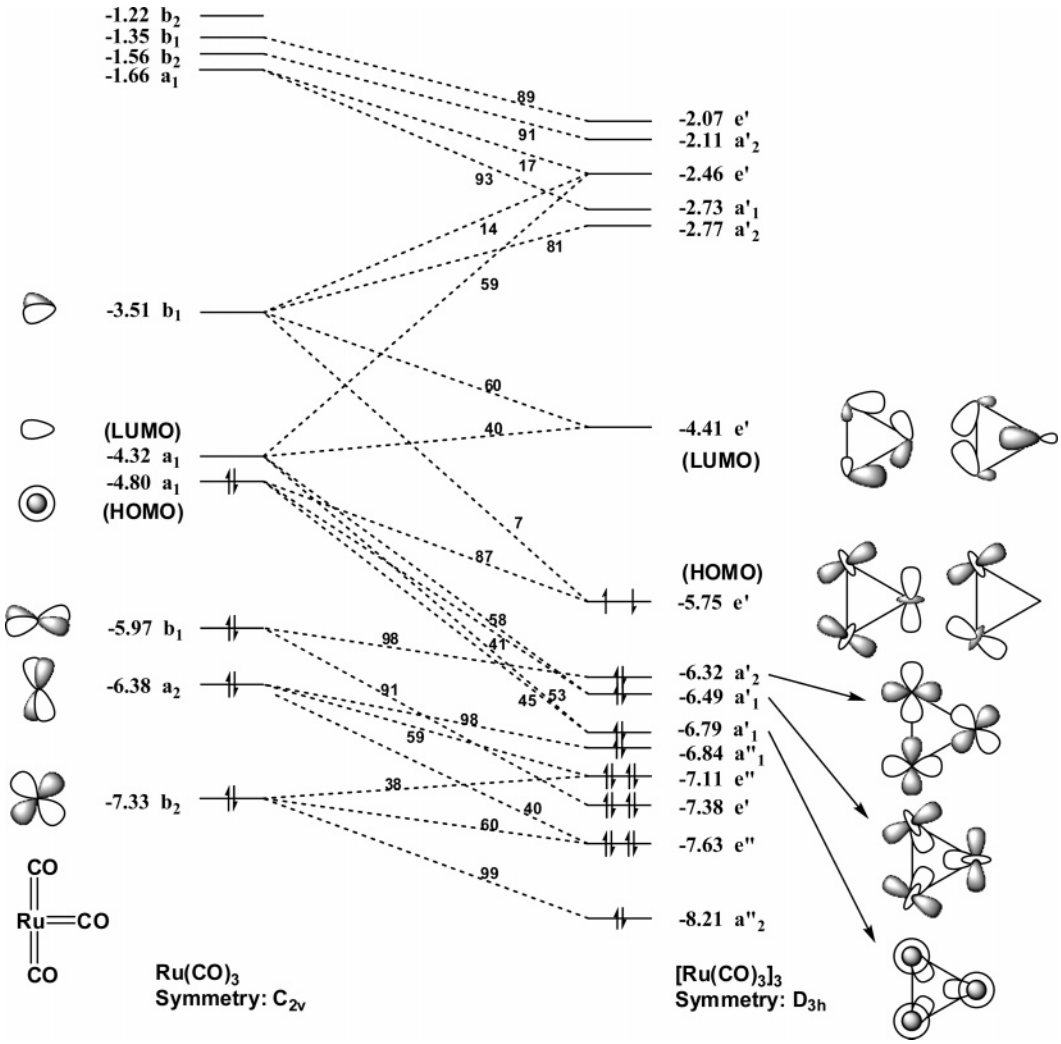

Figure 7. Molecular orbital diagram for the fragment $[Ru(CO)_3]_3$ built from three $Ru(CO)_3$. The numbers on the dotted lines are the percentage of $Ru(CO)_3$ orbitals in the $[Ru(CO)_3]_3$ orbitals. The numbers near the orbital representations are the calculated orbital energies (eV).

Fragment Orbital Analysis for $[Ru(CO)_3]_3$ Built from Three $Ru(CO)_3$ Fragments. The orbital interactions between the $Ru(CO)_3$ fragments in the formation of the inner triangular $[Ru(CO)_3]_3$ fragment are displayed in Figure 7. The geometries of these fragments are from the optimized structure of the Ru_3Sn_3 cluster at D_{3h} symmetry. The $Ru(CO)_3$ fragment has C_{2v} symmetry. Its HOMO and LUMO are both a_1 and have a 0.48 eV gap. Shown on the left of Figure 7 are the principal

Scheme 5

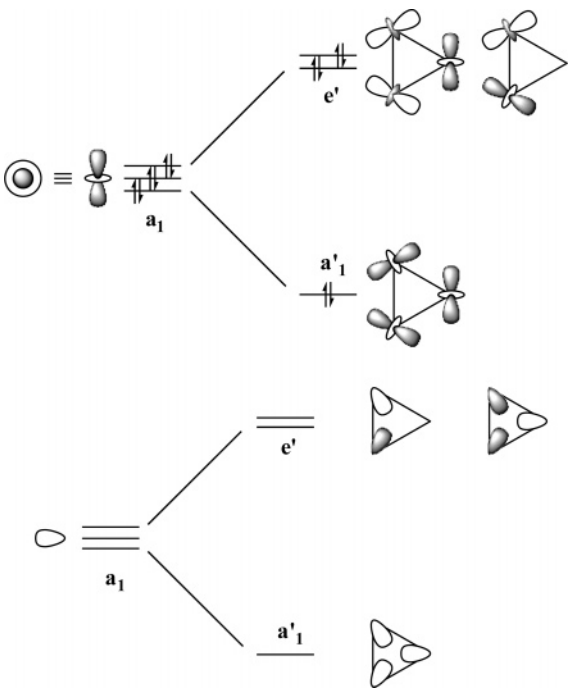

Ru based molecular orbitals and some of the higher lying virtual molecular orbitals. Not shown are the electrons primarily associated with the CO ligands as these lie lower in energy and are involved in Ru−C and C−O bonding, but not in the cluster bonding. $Ru(CO)_3$ is a d^8 system, and the four occupied metal orbitals b_2, a_2, b_1, and a_1 (HOMO) correspond to those expected for a planar (or square-planar) metal complex. The two lowest lying virtual molecular orbitals a_1 (LUMO) and b_1 correspond to the symmetric and antisymmetric molecular orbitals that would each accept an additional electron pair in the formation of a stable 18 e^- complex such as $Ru(CO)_5$. Finally, the higher lying orbitals a_1, b_2, b_1, and b_2 are mainly CO π^* in character. Because of the short Ru−Ru distances (2.99 Å) in the geometry of the $[Ru(CO)_3]_3$ fragment, there are strong interactions between the molecular orbitals of the $Ru(CO)_3$ fragments. These interactions increase the HOMO and LUMO gap of the $[Ru(CO)_3]_3$ fragment to 1.34 eV. The stability of the inner triangular fragment is driven mainly by the interaction of the a_1 HOMO and the a_1 LUMO with some contribution from the b_1 (LUMO+1). This is most easily visualized by considering each orbital separately and how each interacts with the corresponding orbital on its neighboring Ru. As shown in Scheme 5 (left side), the three $Ru(CO)_3$ a_1 HOMOs interact to form a bonding a'_1 (D_{3h}) and an antibonding e'. In a similar situation the three $Ru(CO)_3$ a_1 LUMOs interact to form a bonding a'_1 and an antibonding e' (Scheme 5 right side). If the three pairs of electrons in the a_1 HOMO of the $Ru(CO)_3$ fragments remained in the $[Ru(CO)_3]_3$ fragment molecular orbitals formed from these orbitals, there could be no net bonding. However, the a'_1 orbital formed from the a_1 LUMOs falls below the e' from the (a_1

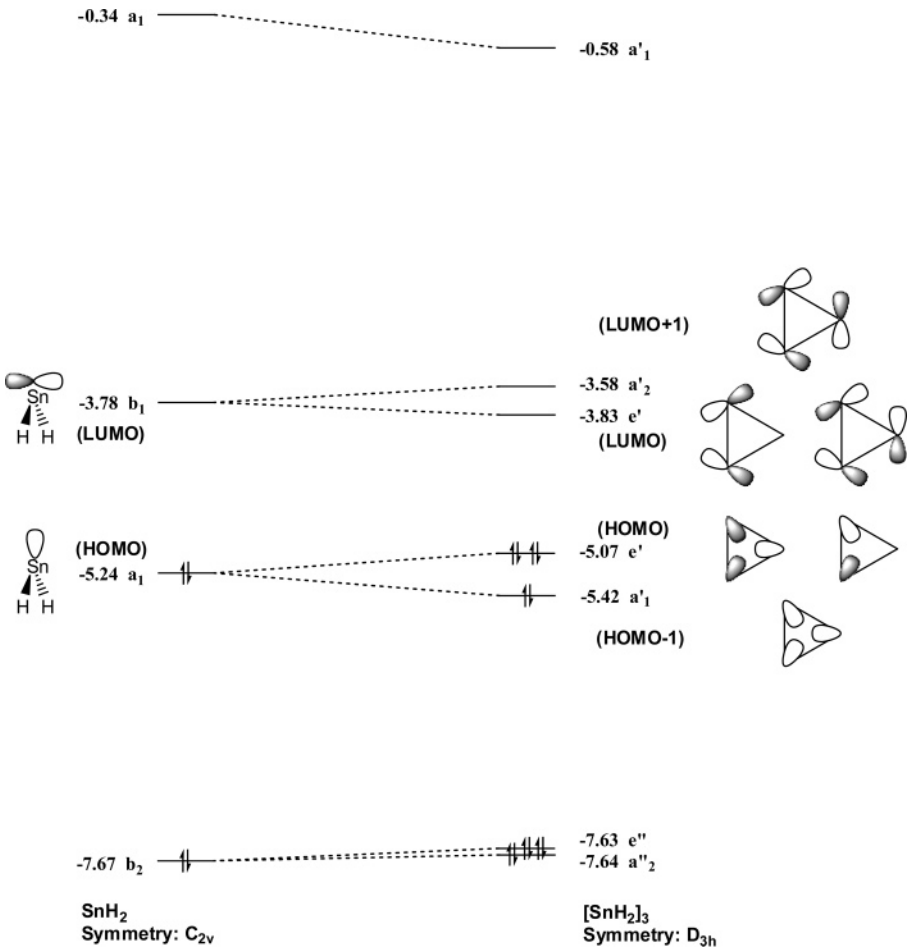

Figure 8. Molecular orbital diagram for the $[SnH_2]_3$ fragment built from three SnH_2. The numbers near the orbital representations are the calculated orbital energies (eV).

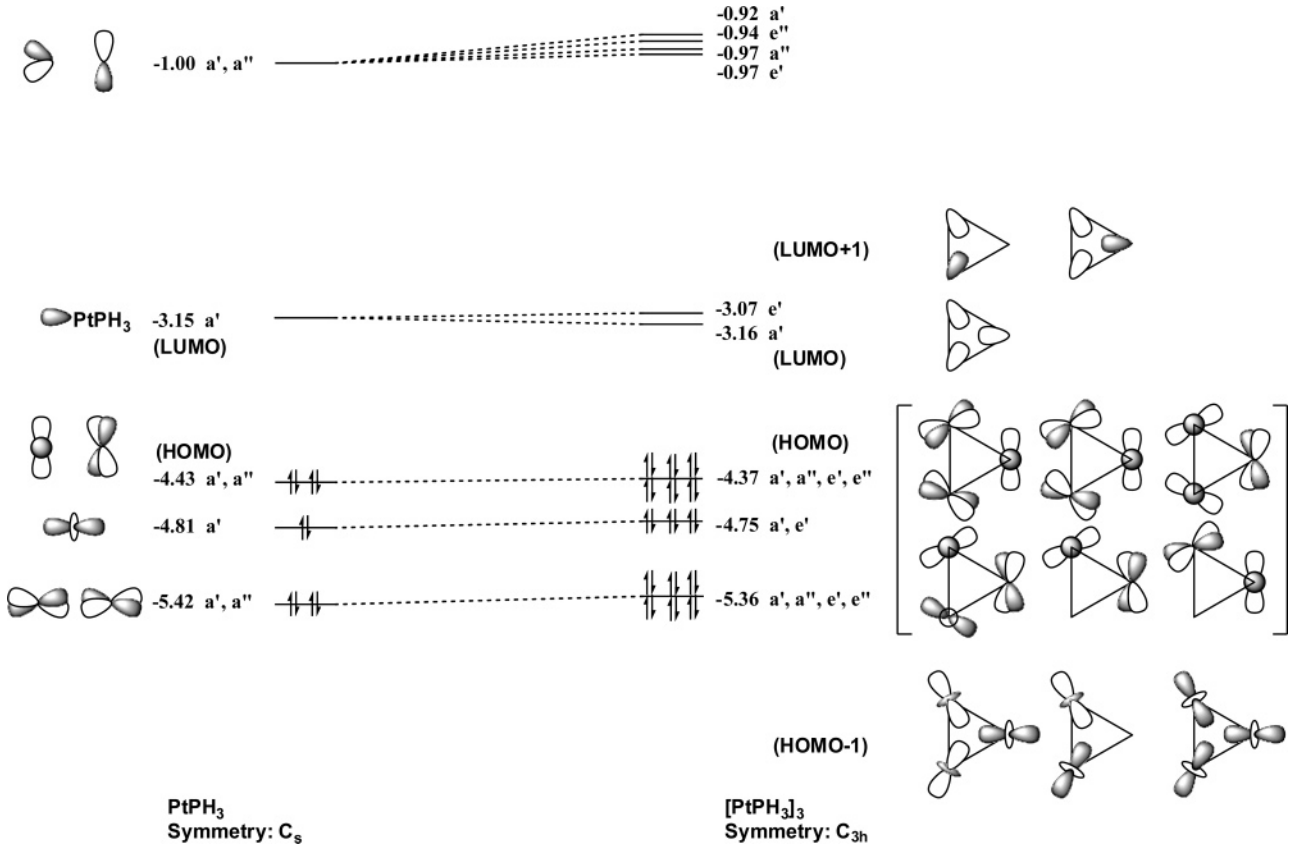

Figure 9. Molecular orbital diagram for the fragment $[PtPH_3]_3$ built from three $PtPH_3$ fragments. The numbers near the orbital representations are the calculated orbital energies (eV).

HOMOs) and one pair of electrons falls into this lower energy orbital. The two in-plane a'_1 (a_1 HOMO) and a'_1 (a_1 LUMO) mix with each other and form the a'_1 molecular orbitals at −6.79 and −6.49 eV. The antibonding e' (a_1 HOMO) is then stabilized by the b_1 $Ru(CO)_3$ orbital and forms the HOMO of the triangular fragment. The LUMO of $[Ru(CO)_3]_3$ is also an orbital which is derived mainly from the LUMO (40%) and LUMO + 1 (60%) of $Ru(CO)_3$. By this analysis we do not intend to imply that this $[Ru(CO)_3]_3$ fragment with its half-filled e' (HOMO) would be stable by itself. In fact, it will require three SnR_2 fragments to stabilize it.

Fragment Orbital Analysis for $[SnH_2]_3$ Built from Three SnH_2 Fragments. The orbital interactions between fragments in the formation of $[SnH_2]_3$ are displayed in Figure 8. The SnH_2 fragment has C_{2v} symmetry. Its HOMO and LUMO are a_1 and b_1 with a 1.46 eV gap. The $[SnH_2]_3$ fragment in the Ru_3Sn_3 cluster has a smaller HOMO and LUMO gap of 1.24 eV, because the Sn atoms in $[SnH_2]_3$ are so distant (5.36 Å) that they only interact weakly. Thus, the orbitals of the triangular fragment $[SnH_2]_3$ are essentially those generated from the symmetry imposed on the three SnH_2 fragments.

Fragment Orbital Analysis for $[PtPH_3]_3$ Built from three $PtPH_3$ Fragments. The orbital interactions between the $PtPH_3$ fragments in the formation of $[PtPH_3]_3$ are displayed in Figure 9. The geometries of these fragments are from the optimized structure of the $Ru_3Sn_3Pt_3$ cluster at C_{3h} symmetry. Since the individual $PtPH_3$ fragments are distorted, they have no symmetry and C_s symmetry was used for their labels. The Pt atoms in the $Ru_3Sn_3Pt_3$ cluster have large (7.42 Å) distances and very weak interactions between them, so the orbital energies of $[PtPH_3]_3$ are very similar to those of $PtPH_3$. The HOMO and LUMO gap of $[PtPH_3]_3$ is only 0.07 eV smaller than that of the $PtPH_3$.

Fragment Orbital Analysis for Ru_3Sn_3 Built from $[Ru(CO)_3]_3$ and $[SnH_2]_3$. The orbital interactions between the $[Ru(CO)_3]_3$ and $[SnH_2]_3$ fragments are displayed in Figure 10. The principal bonding interactions arise from the interaction of the four highest occupied (e' (HOMO), a'_2, a'_1) and the e' (LUMO) of $[Ru(CO)_3]_3$ with the high lying occupied (e' (HOMO), a'_1) and unoccupied (e' (LUMO), a'_2) of $[SnH_2]_3$. The key bonding molecular orbitals (those in-phase contributions not cancelled by out-of-phase occupied orbitals) are the −8.81 a'_1 (mixing of −6.79 a'_1 and −5.42 a'_1); the −8.47 e' (mixing of −5.75 e' and −5.07 e'); the −7.20 e' (mixing of −5.75 e' and −5.07 e'); the −7.00 a'_2 (mixing of −6.32 a'_2 and −3.58 a'_2); and the −6.28 e' (HOMO) (mixing of −4.41 e' and −3.83 e'). The total bonding electron count corresponds to two electrons from each of the fragments, and the remaining electrons on each fragment are either π bonding to the COs or involved in other strong bonds. The key molecular orbitals are plotted in Figure 11.

Fragment Orbital Analysis for $Ru_3Sn_3Pt_3$ Built from Ru_3Sn_3 and $[PtPH_3]_3$. The interactions between the Ru_3Sn_3 and $[PtPH_3]_3$ fragment and the change of orbital energies in the Ru_3Sn_3 cluster with the change of geometry caused by three Pt ligands are displayed in Figure 12. The first and second columns from the left in this figure are the orbital energies of Ru_3Sn_3 at the optimized structure and at the geometry of the final cluster, in which the in-plane CO is bent. This distortion causes only a small change in the molecular orbital energies, but it does reduce the HOMO−LUMO gap by 0.26 eV. The bonding between the Ru_3Sn_3 fragment and the Pt_3 fragment is driven by a number

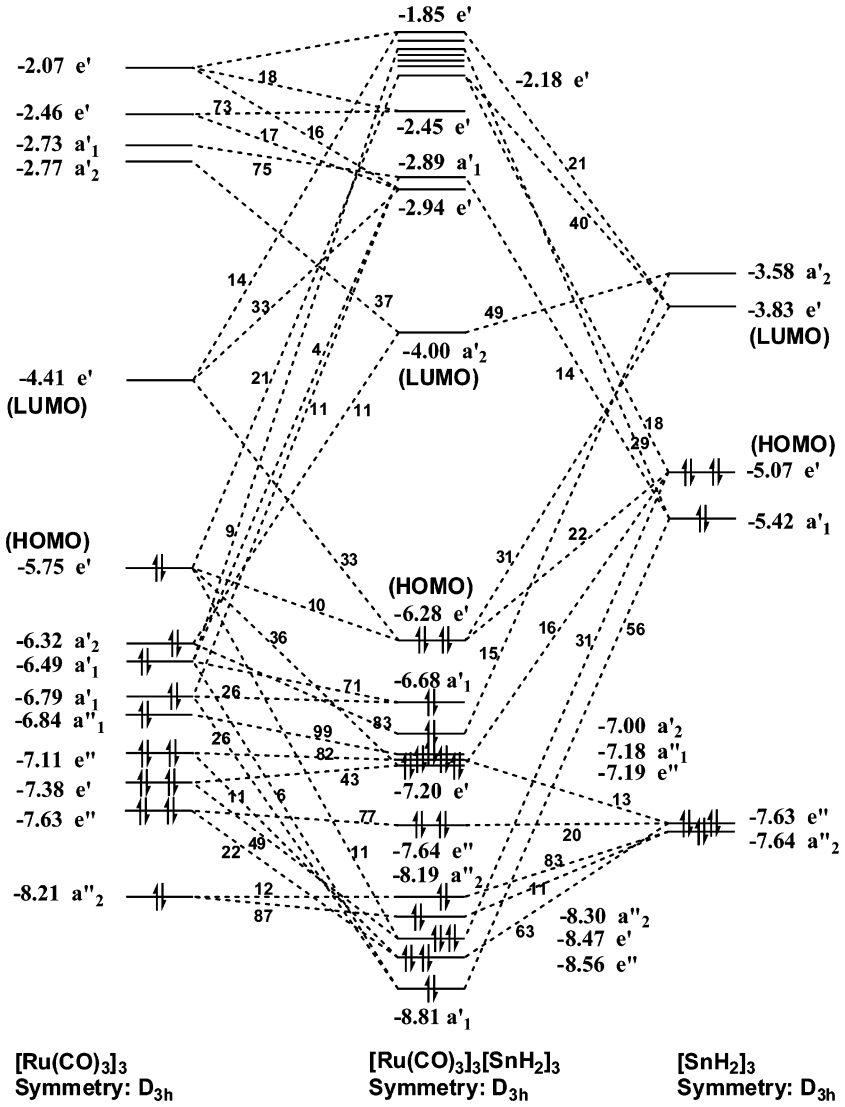

Figure 10. Molecular orbital diagram for the Ru_3Sn_3 cluster built from $[Ru(CO)_3]_3$ and $[SnH_2]_3$. The numbers on the dotted lines are the percentage of the $[Ru(CO)_3]_3$ and $[SnH_2]_3$ fragment orbitals in the Ru_3Sn_3 orbitals. The numbers near the orbital representations are the calculated orbital energies (eV).

of small interactions. The −4.75 a' of the Pt_3 fragment donates electrons to the −4.19 a'(LUMO) of the Ru_3Sn_3 fragment. The low lying Ru_3Sn_3 LUMO and the Pt_3 LUMO and LUMO+1 also stabilize several occupied molecular orbitals. Although the LUMO of the $Ru_3Sn_3Pt_3$ cluster remains about 70% LUMO of the Ru_3Sn_3 fragment, the HOMO of the $Ru_3Sn_3Pt_3$ cluster increases its Pt content to 23% after the attachment of all the $PtPH_3$ units.

Predicted Spectral Transitions. The excited-state energies and their intensities calculated by TDDFT are shown in Table 3. The simulated spectra shown in Figure 6 were produced by the Synspec program.[28] Symmetries and orbital assignments for the high-symmetry Ru_3Sn_3 and $Ru_3Sn_3Pt_3$ clusters are also given in Table 3. Comparison to the experimental results shows excellent agreement.

From Figure 10, the HOMO and LUMO of Ru_3Sn_3 are e' and a'_2 with a 2.28 eV gap. The TDDFT calculations predict a corresponding allowed transition to the E' excited state at 2.666 eV (Table 3). The HOMO−1 orbital of Ru_3Sn_3 is a'_1, and the corresponding transition to the LUMO of a'_2 (A'_2 excited state at 2.813 eV) is forbidden. The remaining low lying excited states of Ru_3Sn_3 are all generated by electronic transitions from occupied orbitals to the LUMO as the energy gap between LUMO and LUMO+1 orbitals of Ru_3Sn_3 is 1.06 eV, much larger than the energy gaps between HOMO and several nearby occupied orbitals. The TDDFT calculations predict a splitting and decrease in the excited-state energies as the $PtPH_3$ fragments are added, ultimately leading to two separate bands in the $Ru_3Sn_3Pt_3$ cluster. The first allowed excitation at 2.113 eV corresponds to E' (−5.24 e' → −3.46 a'), the HOMO−LUMO transition, whose lower energy arises mainly from a decrease in the HOMO−LUMO gap to 1.78 eV caused by a combination of distortion of the in-plane COs to accommodate the Pt and a larger participation of the Pt orbitals in the HOMO than the LUMO. Because the LUMO and LUMO+1 gap is 0.48 eV, 0.1 eV smaller than the HOMO and HOMO−1 gap 0.58 eV, the second allowed excitation at 2.500 eV arises from the transition of −5.24 e' (HOMO) → −2.98 e' (LUMO+1). Thus, the predicted absorption spectra of these clusters split into two separate bands after three Pt units are added.

(28) Irikura, K. K. National Institute of Standards and Technology (NIST), Gaithersburg, MD 20899, U.S.A., 2005.

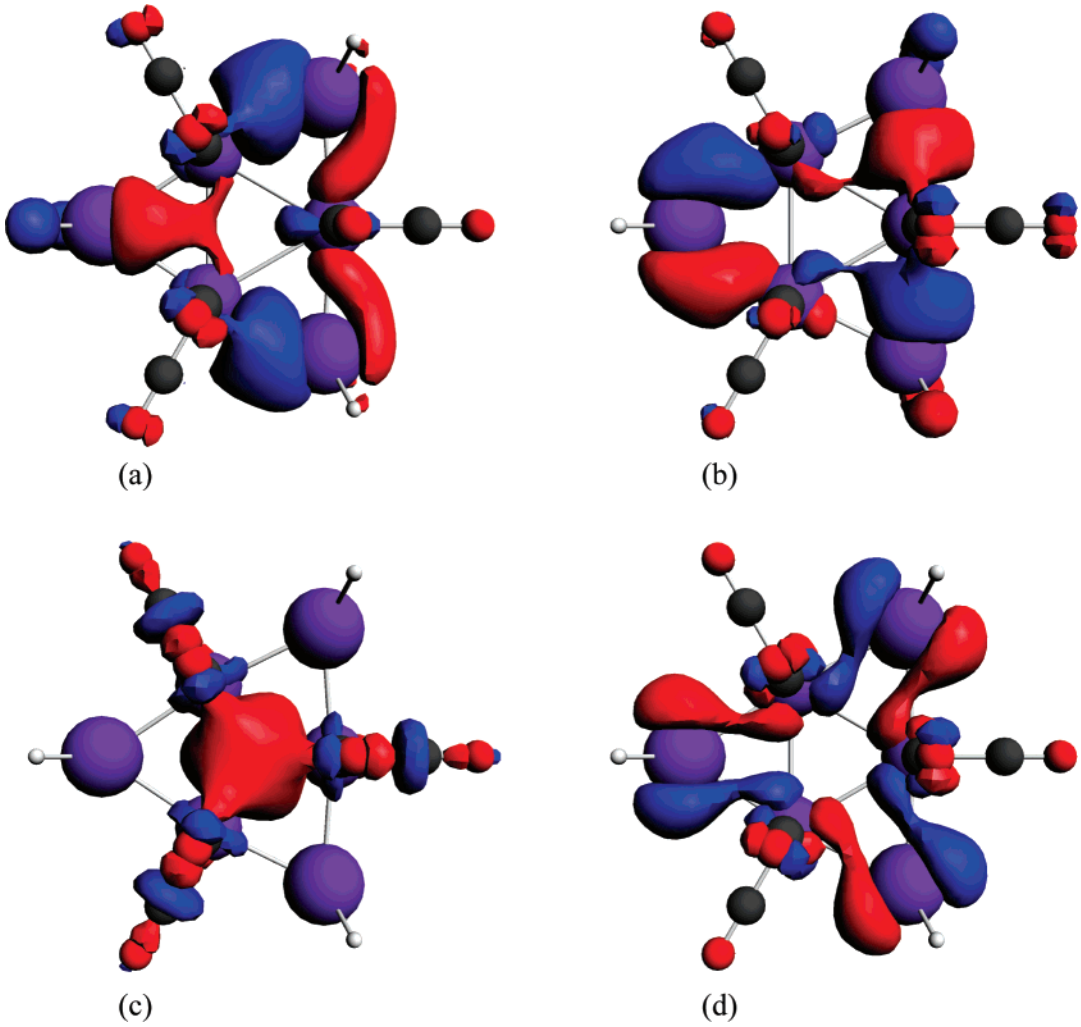

Figure 11. ADFView plots of key molecular orbitals of the Ru_3Sn_3 cluster at D_{3h} symmetry. (a) and (b) are degenerate −6.28 e' (HOMO). (c) −6.68 a'_1 (HOMO-1) orbital. (d) −4.00 a'_2 (LUMO).

Table 3. Vertical Excitation Energies E, Corresponding Oscillator Strengths f, and the Symmetry of the Six Lowest Singlet Excited States of the Ru−Sn−Pt Clusters at Their Optimized Structures

	Ru_3Sn_3 (D_{3h})				$Ru_3Sn_3Pt_1$ (C_1)		
excited states	E (eV)	sym.	f	principal orbital contribution	E (eV)	f	principal orbital contribution
1	2.666	E'	0.0908	HOMO → LUMO	2.367	0.1120	HOMO → LUMO
2	2.666	E'	0.0908	HOMO → LUMO	2.588	0.0353	HOMO−1 → LUMO
3	2.813	A_2'	0.0000	HOMO−1 → LUMO	2.657	0.0298	HOMO → LUMO+1
4	3.293	A_1'	0.0000	HOMO−2 → LUMO	2.670	0.0285	HOMO−2 → LUMO
							HOMO → LUMO+1
5	3.435	E''	0.0000	HOMO−2 → LUMO	2.817	0.0001	HOMO−3 → LUMO
6	3.435	E''	0.0000	HOMO−4 → LUMO	2.864	0.0067	HOMO−4 → LUMO
	$Ru_3Sn_3Pt_3$ (C_{3h})				$Ru_3Sn_3Pt_2$ (C_1)		
excited states	E (eV)	sym.	f	principal orbital contribution	E (eV)	f	principal orbital contribution
1	2.113	E'	0.0869	HOMO → LUMO	2.148	0.1046	HOMO → LUMO
2	2.113	E'	0.0869	HOMO → LUMO	2.352	0.0786	HOMO−1 → LUMO
3	2.440	A'	0.0000	HOMO → LUMO+1	2.507	0.0218	HOMO → LUMO+1
4	2.500	E'	0.0287	HOMO → LUMO+1	2.547	0.0057	HOMO−2 → LUMO
5	2.500	E'	0.0287	HOMO → LUMO+1	2.622	0.0067	HOMO−3 → LUMO
6	2.520	A'	0.0000	HOMO−1 → LUMO	2.662	0.0014	HOMO−4 → LUMO

Our calculations show that the absorption maximum for the model structures for **13**, **14**, **15**, and **16** at 465, 508, 556, and 585 nm differ only nominally, 4−18 nm, from the experimental values of 474, 490, 552, and 576 nm. Since these calculations are for simplified model molecular systems, the differences compared to experimental values may be caused by the changes of the electronic structures due to the simplification. The largest difference occurs for $Ru_3Sn_3Pt_1$, which shows a higher experi-

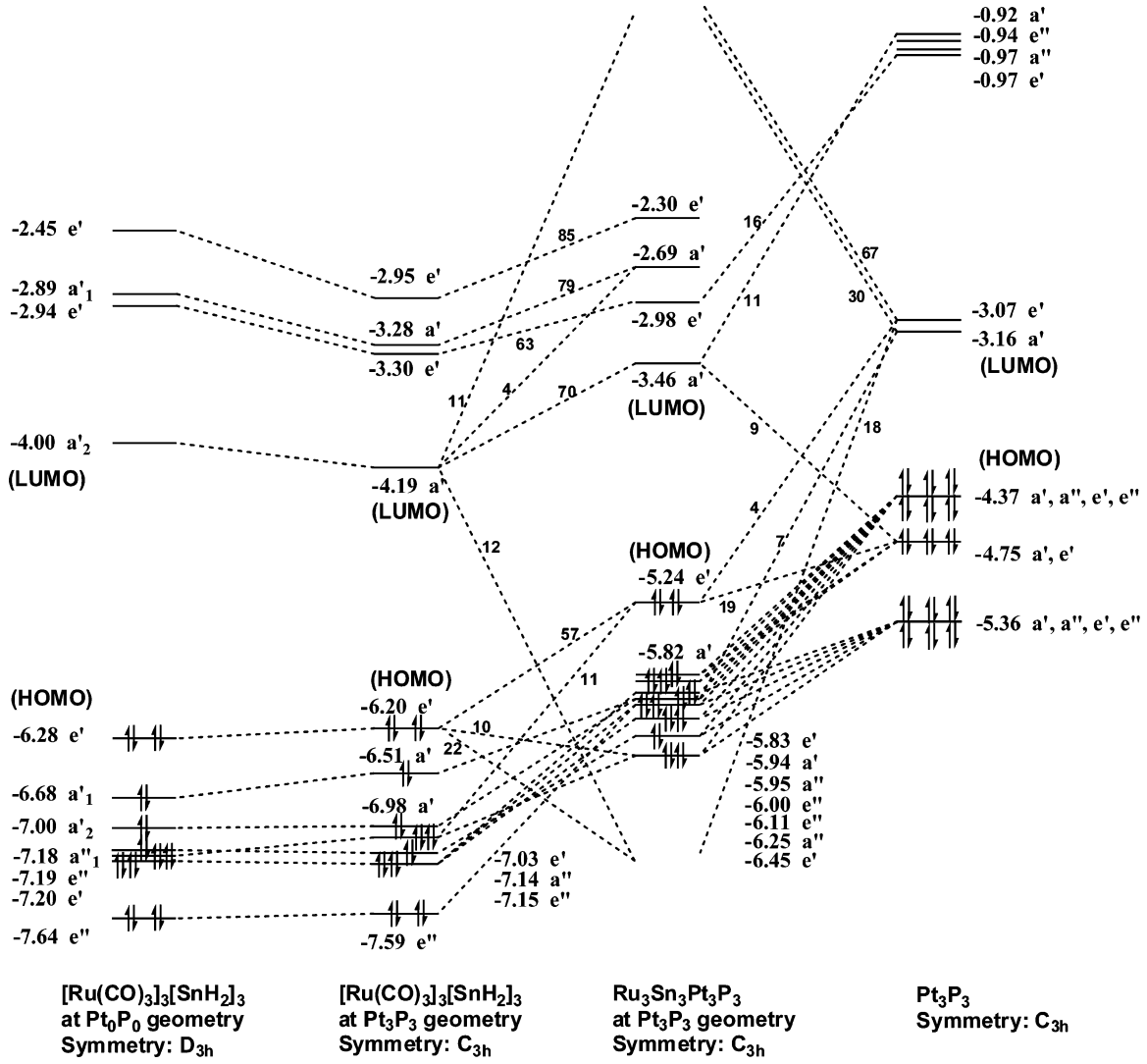

Figure 12. Molecular orbital diagram for the $Ru_3Sn_3Pt_3$ cluster built from Ru_3Sn_3 and $[PtPH_3]_3$. The numbers on the dotted lines are the percentage of the Ru_3Sn_3 and $[PtPH_3]_3$ fragment orbitals in the $Ru_3Sn_3Pt_3$ orbitals. The numbers near the orbital representations are the calculated orbital energies (eV).

Scheme 6

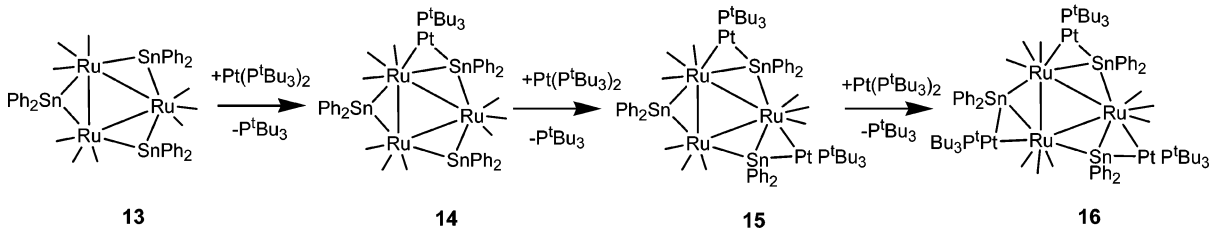

mental value in part because of a rising background which appears to increase the intensity of the higher energy transitions. Overall, the calculations are in excellent agreement with the experimental spectra. In the simulated spectra, the Ru_3Sn_3 and $Ru_3Sn_3Pt_3$ clusters have a little higher peak intensity than that of the $Ru_3Sn_3Pt_1$ and $Ru_3Sn_3Pt_2$ clusters. This increase in intensity should be due to the degeneracy of the *e′* (HOMO) of Ru_3Sn_3 and $Ru_3Sn_3Pt_3$. Correspondingly, the simulated spectra also show a larger bandwidth for $Ru_3Sn_3Pt_1$ and $Ru_3Sn_3Pt_2$ because they have no symmetry and more allowed transitions.

For compound **13**, it is clear that its experimental spectrum has only one absorption peak at wavelengths longer than 400 nm. For the other three complexes, the experimental spectra have a wider absorption band and show evidence of some higher energy transitions at wavelengths shorter than that for the main peak. Not all of these phenomena are reflected in our simulated spectra because we only calculated six singlet excited states for each of these clusters due to the limitation of computational resources.

Summary

A series of new extended two-dimensional multimetallic cluster complexes have been prepared by the addition of one to three $Pt(PBu^t_3)$ groups to the Ru−Sn bonds of the complex **13**; see Scheme 6. All three platinum containing products **14**−**16** are $Pt(PBu^t_3)$ adducts of **13** formed by the sequential addition of a $Pt(PBu^t_3)$ group to a Ru−Sn bond of the cluster of **13**. The

process seems to be a fairly simple one. A PBu^t_3 ligand is eliminated from the $Pt(PBu^t_3)_2$ reagent, and the resultant $Pt(PBu^t_3)$ group is simply added to an Ru−Sn bond. No ligands are eliminated from **13**. The addition of $Pt(PBu^t_3)$ groups to **13** is viewed as a simple Lewis acid/Lewis base type association process. The $Pt(PBu^t_3)$ group is the Lewis acid, and Ru−Sn bond is the electron pair donor. Detailed molecular orbital calculations have shown that the HOMO in compound **13** is metal−metal bonding in character and is dominated by ruthenium−tin interactions. As $Pt(PBu^t_3)$ groups are added to the cluster of **13**, the principal UV−vis absorption of the complexes shifts progressively to longer wavelengths. These absorptions and their shifts have been explained by employing TDDFT calculations that have revealed a lowering of the HOMO−LUMO energy gap due to interactions of the platinum atoms with the HOMO and LUMO of the complexes that are concentrated on the Ru_3Sn_3 core of the molecules.

Acknowledgment. This research was supported by the Office of Basic Energy Sciences of the U.S. Department of Energy (DE-FG02-00ER14980), National Science Foundation (CHE-0518074 and DMS-0216275), Welch Foundation (A0648), and the USC Nanocenter. We thank Mr. John Stone for assistance with the UV−vis measurements. Dedicated to the memory of Professor F. A. Cotton.

Supporting Information Available: Complete refs 14 and 21 and CIF files for each of the structural analyses. This material is available free of charge via the Internet at http://pubs.acs.org.

JA074527O